Full Length Article

The Hyperion-II radio-frequency oxygen ion source on the UCLA *ims*1290 ion microprobe: Beam characterization and applications in geochemistry and cosmochemistry

Ming-Chang Liu*, Kevin D. McKeegan, T. Mark Harrison, George Jarzebinski, Lvcian Vltava

Department of Earth, Planetary, and Space Sciences, UCLA, United States

ABSTRACT

A radio-frequency plasma ion source, the Hyperion-II, has been commissioned on a CAMECA *ims*1290, a high resolution/high transmission secondary ion mass spectrometer at UCLA. Performance characteristics (e.g., beam density, spot size, etc.) of the primary oxygen beam are documented and application to isotopic analyses requiring high lateral resolution with high secondary ion transmission are described. The Hyperion source delivers on average 10 times and 6 times the current density delivered by the CAMECA duoplasmatron for $^{16}O^-$ and $^{16}O_2^-$ beams, respectively. This significantly enhanced current density allows for reduction of the analytical spot size by at least a factor of three while maintaining the beam intensity, making it possible to perform isotopic measurements at smaller scales without sacrificing analytical precision. In addition, the smaller Hyperion beam spot size also reduces the crossover size and spherical aberrations in the secondary ion optics, thereby improving secondary ion transmission at mass resolving power of 3000–12,000 by 25–80% compared to that achieved with a duoplasmatron.

© 2017 Elsevier B.V. All rights reserved.

1. Introduction

Secondary ion mass spectrometry (SIMS) has become a widely applied technique for chemical and isotopic analysis of geological, biological, and synthetic samples. For certain elements that more readily produce positive secondary ions (e.g., Mg, Ca, Ti, Pb, U), an electronegative primary ion beam is required for higher ionization yields. In all geochemical/cosmochemical SIMS laboratories, an O^- or O_2^- beam generated by a hollow-cathode duoplasmatron is used. This type of oxygen ion source has been in use for several decades, but it nevertheless has several disadvantages compared to a Cs^+ gun, the most commonly used source on CAMECA SIMS instruments for generating electropositive primary ions. First, the duoplasmatron has a lower beam brightness (expressed in $mA\,cm^{-2}\,sr^{-1}$) and a larger energy spread ($\sim$10–15 eV) than the Cs^+ source ($\sim$1 eV for the energy spread) [1]. This results in lower spatial resolution (i.e., a larger spot size) for an oxygen primary ion beam compared to a Cs^+ beam of the same beam intensity, potentially limiting certain isotopic analyses requiring positive secondary ions. Second, the duoplasmatron generates ions in a low-pressure ($\sim$2 × 10^{-5} mbar) magnetically confined plasma and the extracted primary ion beam current depends critically on many parameters, such as gas pressure, position of the intermediate electrode and the quality of Ni cathode. The resulting beam intensity varies on a short term, typically ±1% over ten minutes, and can vary much more significantly over hours to days depending on how those parameters are optimized. Moreover, during the generation of plasma, the cathode is subjected to corrosion, which leads to the decreased beam stability and eventual failure of the duoplasmatron after $\sim$200 h of use. Therefore, frequent maintenance of this source, requiring instrument shutdown and partial venting, is necessary.

Recently, Oregon Physics, LLC developed a second-generation radiofrequency (RF) plasma ion source for CAMECA SIMS instruments (including the *ims*-series and the NanoSIMS), known as the Hyperion-II. The imaging performance characteristics of an oxygen beam from a Hyperion-II source mounted on a NanoSIMS 50L have been recently reported [2]. With the Hyperion ion source, $^{16}O^-$ primary beam spot sizes as small as $\sim$40 nm could be realized, comparable to the best focus achievable with a Cs^+ beam on a NanoSIMS.
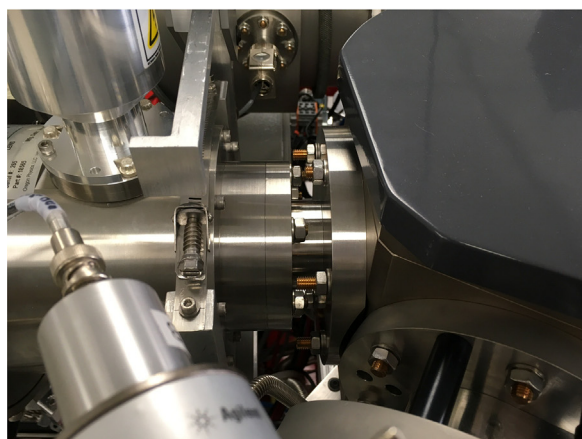
On ion microscope (CAMECA IMS-series) SIMS instruments (especially the *ims*1200 series), utilization of a primary ion beam
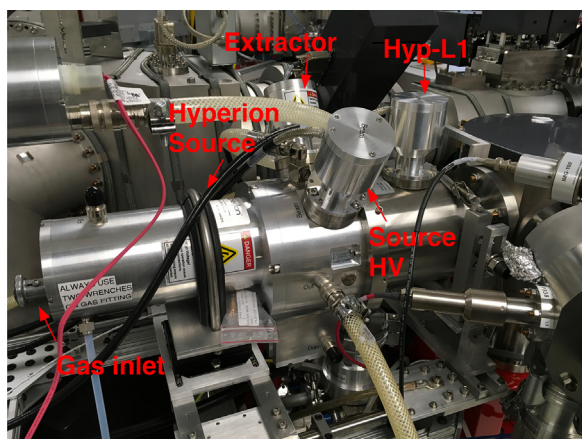
Fig. 1. The mounting of the Hyperion-II source on the UCLA *ims*1290. Via a conflat flange (φ = 11.2 cm), the source is directly mated to the PBMF to be better supported by the structure.

tens of nm in diameter for ion imaging work is not common practice. Instead, high precision (defined as sub-permil for major elements, and permil level for certain minor or trace elements) isotopic analysis is often sought by isotope geochemists and cosmochemists. To obtain data at the desired precision, an $^{16}O^-$ beam intensity of at least ~10–30 nA is typically required to generate sufficient secondary ion intensities for accurate current measurements by Faraday cups [3–5] or to reach sufficient counting statistics for ion counting [6,7]. With a duoplasmatron, such currents result in spot sizes in the range ~15–50 μm, significantly limiting spatial resolution for many applications. Therefore, reducing the spot size while maintaining the same beam intensity would be a highly desirable development.

The UCLA *ims*1290, installed and commissioned in late 2015, is a CAMECA *ims*1280HR equipped with a Hyperion-II source. The instrument is the second large radius SIMS on which a Hyperion source has been mounted,[1] however the configuration of the UCLA *ims*1290 is unique. On the UCLA *ims*1290, the Hyperion-II source replaces the duoplasmatron, and is directly mated to the Primary Beam Mass Filter (PBMF) in place of the Cs source so that it can be better supported by a custom-made structure (Fig. 1). The ion source incorporates an Einzel lens (Hyp-L1) and two pairs of deflectors (D1x and D1y), allowing for steering the primary beam in both

X and Y directions before the Hyp-L1 lens and centering the beam in the flight tube of the PBMF. One limitation of this mounting method is that the D2 deflectors that were originally housed in the duoplasmatron block are removed, making it difficult to center the primary ion beam in the y-direction on lens L2. However, as shown in the results section, the system has enough flexibility such that practical effects on the beam density and performance are minimal.

The purpose of this study is to evaluate the beam characteristics achievable with a Hyperion-II source mounted on the UCLA *ims*1290 ion microprobe. We document beam density, stability, and minimum spot sizes that have been achieved for different analytical conditions. We also illustrate the effects of analytical spot size on transmission of secondary ions at high mass resolution, which is important for many applications including Pb isotopic analyses of zircon and other accessory minerals [8,9], and the applicability of the high-density $^{16}O^-$ beam to small spot, high precision Mg isotopic analysis, a system of great interest in cosmochemistry.

2. Experimental methods

2.1. Beam density assessment

In assessing beam density, it is necessary to measure the intensity of ions delivered to the sample surface as a function of the analytical spot size. We measured diameters of critically focused (Gaussian) $^{16}O^-$ beams of various intensities (0.05–70 nA) by using secondary ion imaging. For ion beam currents ≤20 nA, spot sizes were estimated by acquiring a series of scanning ion images on a resolution standard. We utilized the "CAMECA Si-Ta tuning sample", a tantalum substrate with an image pattern formed by silicon deposited on the surface. Since the spatial resolution in a scanning ion image is limited by the primary beam size, one can directly gauge the spot diameter by finding the minimum spacing between Si bars that can be resolved in an ion image. A different method must be employed for the large diameter ion beams, corresponding to 45 nA and 70 nA with the Hyperion-II. For these high intensity beams, spot sizes were estimated by rastering a 250 μm × 250 μm square on an area with a sharp contrast in ion emission (a Si-Ta interface), and then imaging in the inner 150 μm × 150 μm area. The acquired ion image was analyzed by the off-line CAMECA Spot-Shape program to obtain horizontal and vertical line profiles across the image plane, from which one could determine the spot size according to the distance between 16% and 84% of peak intensity. In addition to $^{16}O^-$ primary ions, the spot size of a 5 nA $^{16}O_2^-$ beam was also evaluated in the same way as for the low intensity (<20 nA) $^{16}O^-$ beams.

2.2. Relative transmission vs. mass resolution

To evaluate the relative secondary ion transmission at different values of mass resolution, we rastered a 25 μm × 25 μm square on a Si wafer with a 0.5 nA $^{16}O^-$ beam (φ ~ 1 μm). Dynamic transfer optics were set at 100% and a 150 μm contrast aperture was used to limit the crossover and minimize secondary aberrations due to ions emitted far from the optical axis. Intensities of $^{28}Si^+$ at six mass resolution settings, M/ΔM = 3000, 4000, 5000, 6000, 9000, and 12,000 (ΔM is defined as the width of the peak at 10% height), were recorded by using the FC2 Faraday cup, and then were normalized to the intensity measured with the entrance slit wide open.

2.3. Lead sensitivity

Lead isotope sensitivity was evaluated under the analytical condition in which U-Pb or Pb–Pb dating of zircon would be performed

---

[1] The first is at the National Institute of Standards and Technology.
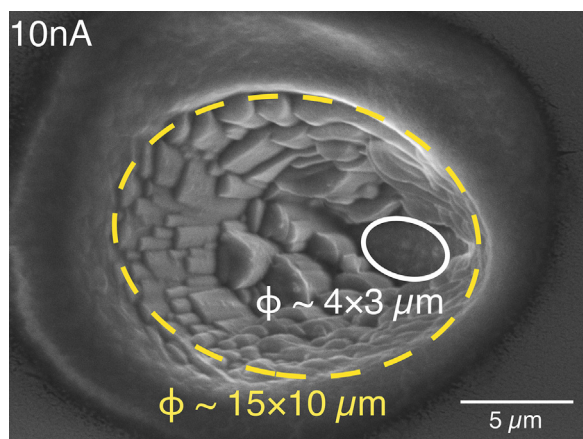
Fig. 2. An ion probe crater sputtered with a 10 nA for 1 h to enhance the pit geometry. The real spot size is around 4 × 3 μm, consistent with the assessment by using ion imaging. The much larger spot size (∼15 × 10 μm) on the surface is due to extended sputtering.

Table 1
Current densities (mA cm^{-2}) measured at different primary beam intensities (nA).

Primary beam current (nA)	Spot area (μm^2)	Current density (mA cm^{-2})
0.05	<0.785	>6
0.1	<0.785	>13
0.2	<0.785	>26
0.5	∼0.785	∼63
1	∼1.54	∼65
10	∼9.62	104
20	∼19.63	102
45	∼66	∼68
70	∼96	∼74
5 (O_2^-)	∼15.9	31

[9]. A polished, epoxy-mounted 91500 zircon grain (Pb concentration = 13.8 ppm) [10] was sputtered with a 10 nA $^{16}O^-$ beam (φ ∼ 4 μm). Secondary ion intensities of $^{206}Pb^+$ were recorded with or without oxygen flooding, and in the form of mass spectra at mass 206 to determine mass resolution (defined by peak width at 10% intensity).

2.4. Magnesium isotope analysis

Magnesium isotopic measurements were performed by following a method described previously [4] with slight modifications. A suite of terrestrial standards (Burma spinel, San Carlos olivine, San Carlos pyroxene, and an isotopically normal synthetic glass of fassaite composition known as "P0") were analyzed under three different primary beam intensity settings: 5, 10 and 15 nA, to which the corresponding spot sizes are approximately 2, 3, and 4 μm, respectively. Fig. 2 shows an example of a crater made with a 10 nA beam sputtering for 1 h to enhance the pit geometry. The beam came onto the sample surface at an angle, so that the crater is asymmetrically conical in shape. The diameter of the pit at the bottom, representing the actual spot size, is approximately 4 × 3 μm, consistent with that derived from ion imaging. The larger diameter (∼15 × 10 μm) on the surface is a result of extended sputtering. The pit depth is ∼6 μm, determined with a MicroXAM profilometer. With those intensities, the resulting secondary ion signals are intense enough to be measured by multiple Faraday cups (FCs) simultaneously. In contrast, if one were to use such a small beam generated by a duoplasmatron for the same analysis, the secondary intensities would be too low for FCs and hence would not yield high-precision results. The total analysis time per spot consists of 60 s of "pre-sputtering" to achieve sputtering equilibrium and 50 s (5 s/cycle for 10 cycles) for data acquisition. $^{24}Mg^+$, $^{25}Mg^+$ and $^{26}Mg^+$ were collected by using L2′ (10^{10} Ω), C (10^{11} Ω), and H1 (10^{11} Ω) FC detectors, respectively. During pre-sputtering, the backgrounds of FCs, which only contributed <1% to the total signals, were measured and corrected for in the data reduction. The mass resolution (M/ΔM) was set at 2400 (corresponding to the first exit slit on the multicollector array) to separate doubly charged ion interferences ($^{48}Ca^{2+}$ and $^{48}Ti^{2+}$) from the peaks of interest. Although $^{24}MgH^+$ was only partially resolved from $^{25}Mg^+$ under such mass resolution, the vacuum condition (pressure ≤1 × 10^{-9} Torr) in the analysis chamber made the hydride contribution negligible (<0.05‰). The deviation of measured isotopic ratios from the reference values ($^{25}Mg/^{24}Mg = 0.12663$ and $^{26}Mg/^{24}Mg = 0.13932$ [11]) is expressed in delta-notation [12] as:

$$\delta^i Mg = \left[\frac{\left(^iMg/^{24}Mg\right)_m}{\left(^iMg/^{24}Mg\right)_{ref}} - 1 \right] \times 1000$$

where i = 25 or 26, and m stands for "measured". The instrumental mass fractionation factor β, derived from linear regression through all data points in $\delta^{25}Mg$–$\delta^{26}Mg$ space, varies slightly with the primary beam intensity and spans between 0.510 and 0.514. This range is comparable to those obtained on other *ims*1200 series ion probes [4,5,13]. A main application of Mg isotope analysis in cosmochemistry is to understand the abundances of short-lived ^{26}Al ($t_{1/2} = 0.7$ Myr) in the early Solar System objects through the excess in its daughter isotope ^{26}Mg ($\equiv \Delta^{26}Mg^*$), i.e., the horizontal deviation from the mass-dependent fractionation line. This quantity can be calculated by following the equations recommended in [12]: $\Delta^{26}Mg^* = \delta^{26}Mg - [(1 + \delta^{25}Mg/1000)^{1/\beta} - 1] \times 1000$. A synthetic glass of fassaite composition doped with a 10.3 permil excess in ^{26}Mg, referred to as P10, was measured as an unknown to check the accuracy of analysis.

3. Result and discussion

3.1. Ion imaging: spot size and beam density

The results of scanning ion imaging resolution tests as a function of beam current are summarized in Fig. 3 and Table 1. The maximum beam diameter on the sample surface can be estimated from the resolution of the ion images. For example, with a 20 nA $^{16}O^-$ beam the 5 μm gap between two horizontal Si bars is clearly resolved, but is less obvious between vertical bars, indicating a spot comparable to or slightly smaller than 5 μm. This can be translated to a current density of ∼100 mA cm^{-2}, which is about 10 times better than the CAMECA specification for a duoplasmatron generated $^{16}O^-$ beam and consistent with our experience. The best current densities are achieved for $^{16}O^-$ beams in the 10–20 nA range, although similar current densities (in the range of ∼70 mA cm^{-2}) are obtained for other primary beam currents between 1 and 70 nA (Fig. 4). This enhancement factor is lower than the ∼16 times improvement documented on the NanoSIMS [2], but the discrepancy could simply reflect the difference in ion optics of the primary columns of *ims* series and NanoSIMS ion probes, such as primary beam incidence angle and distance between sample and objective lens, which are designed to enhance beam focusing (and thus spatial resolution) in the NanoSIMS.

The practical advantages of the Hyperion-II source can be appreciated by considering common geochemical or cosmochemical applications. For a current of ∼10–30 nA typically required to perform high precision isotopic analysis for major elements using multiple FCs (e.g., Mg or Si isotopes) or for minor/trace elements using EMs (e.g., U-Pb dating), one is able to reduce the spot size
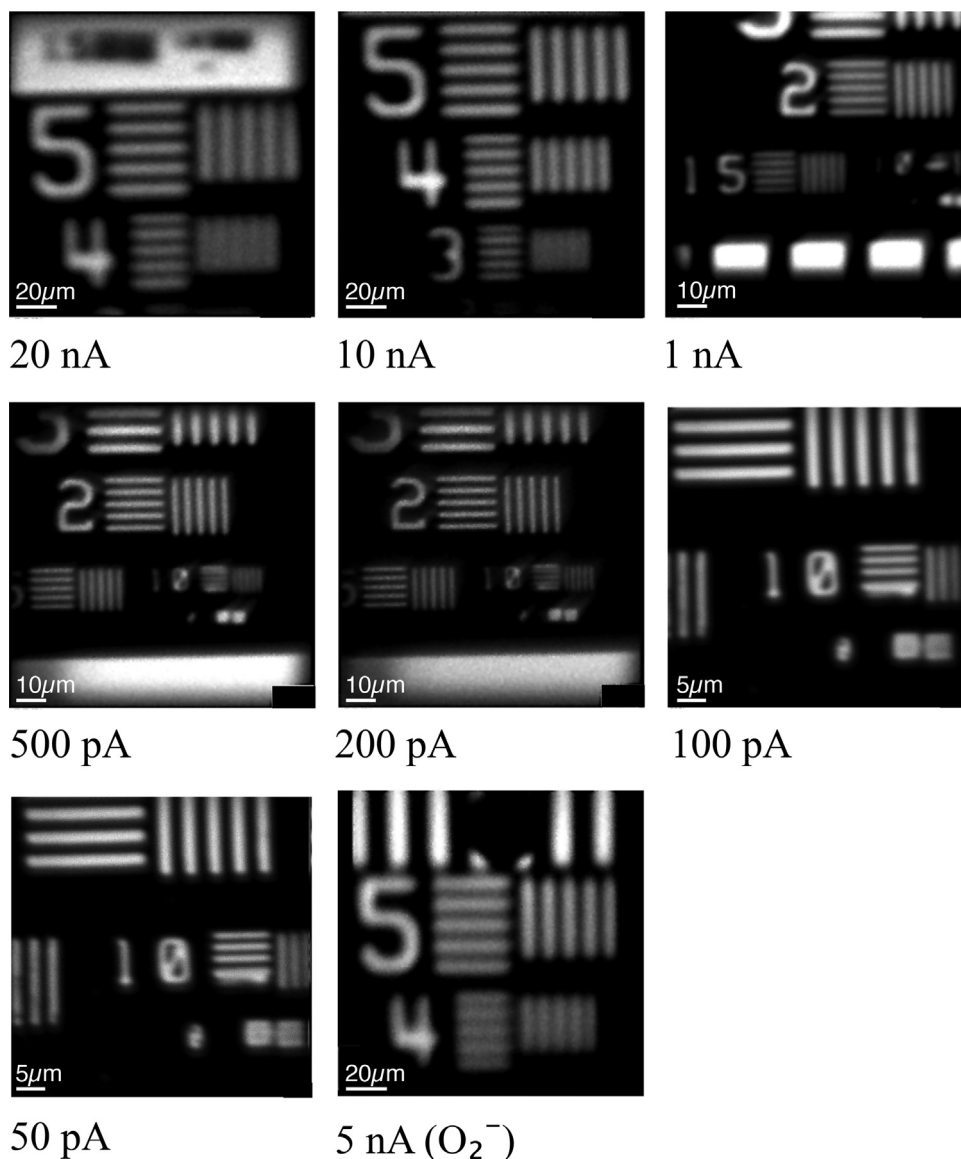
Fig. 3. Scanning ion images of $^{28}Si^+$ (or $^{30}Si^+$) sputtered by $^{16}O^-$ beams of various intensities. The Si is deposited on a Ta substrate in a pattern with line spacing in micrometers indicated by the adjacent numbers. Because lateral resolution of a scanning ion image depends primarily on beam size, the maximum beam diameter can be estimated at various primary beam intensities by the minimum line spacing that can be resolved in an image. In the 100 pA and 50 pA images, the "10" in the image should read "1.0", i.e., 1 μm.

from 25–50 μm to only a few μm, allowing for measurements at much finer spatial scale without sacrificing any analytical precision. Viewed in another way, for a given spot size, ion intensities can be increased by around a factor of 100. While the ionization yields remain unchanged, data acquisition rates are enhanced by the same factor. This is crucial for measurements that are not sample-limited but instead require high secondary ion signals on all isotopes for simultaneous collection by using multiple FCs. In addition, analysis time required to achieve a given precision can be significantly reduced, improving sample throughput.

The 5 nA $^{16}O_2^-$ beam tested here has around 5 μm spatial resolution, equivalent to having a current density of ~25 mA cm^{-2}, which is comparable to the CAMECA specification of >20 mA cm^{-2} for the Hyperion source and 6 times higher than the duoplasmatron value of 4 mA cm^{-2}. Although an $^{16}O_2^-$ beam is not often used for quantitative isotope analysis, it is nevertheless very useful for depth profiling because it improves depth resolution by reducing the implantation depth for a given impact energy of the primary ion beam. The $^{16}O_2^-$ ion beam also yields a higher secondary ion sen-

sitivity (cps/ppm/nA) for Pb$^+$ than does $^{16}O^-$ because of increased oxygen in the sputtering volume [9] (e.g., $^{16}O_2^-$ and $^{16}O^-$ beams result in Pb sensitivity with oxygen flooding of ~21 cps/ppm/nA and ~13 cps/ppm/nA, respectively [14]), On the other hand, at a given current an O_2^- primary beam is ~2 times larger in diameter than an $^{16}O^-$ beam, making it less suitable for some measurements which require very high spatial resolution. Still, the size of a Hyperion $^{16}O_2^-$ beam is ~1.5–2.5 times smaller than an equivalent intensity $^{16}O_2^-$ or $^{16}O^-$ beam generated by the duoplasmatron. With such an improvement in beam density delivered by the Hyperion-II source relative to the duoplasmatron, it can be expected that an $^{16}O_2^-$ beam will be used more often for quantitative isotope analysis.

3.2. Relative transmission at different mass resolution

The relative secondary ion transmission (in percent) as a function of mass resolution is shown in Fig. 5; also shown are data reported for the UCLA *ims*1270 as measured with the duoplasmatron [15]. It can be seen that the relative transmission at any mass
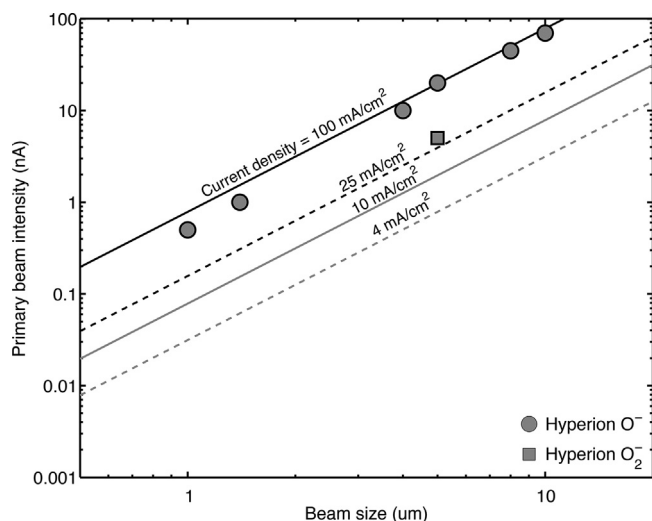
Fig. 4. The current density plot. Filled circles are $^{16}O^-$ beams at different intensities; the filled square is a 5 nA $^{16}O_2^-$ beam. The black and gray solid lines represent the CAMECA-guaranteed $^{16}O^-$ current densities of 100 mA cm^{-2} and 10 mA cm^{-2}, respectively, for the Hyperion and duoplasmatron (Peres 2017, pers. comm.). The dashed lines are 10 mA cm^{-2} and 4 mA cm^{-2} for the Hyperion (solid) and duoplasmatron (dashed) $^{16}O_2^-$ beams.
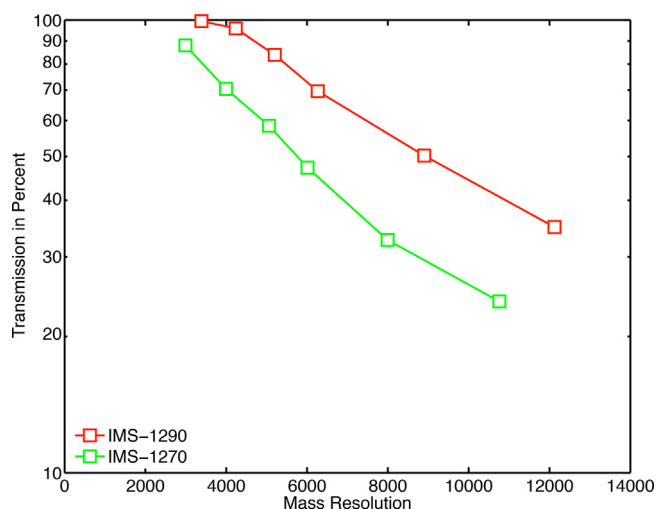

Fig. 5. Relative transmission at different mass resolution. See text for analytical condition. The plot clearly shows that the Hyperion-equipped ims1290 surpasses the conventional ims1270 in relative secondary ion transmission by 25–80%.

resolution on the IMS-1290 using the Hyperion source is significantly improved over the ims1270 by 25–80%, even though the accelerating voltage and transfer optics of both instruments where set to the same nominal values. The main difference, of course, is that the Hyperion source produces a significantly smaller primary beam spot which results in a smaller crossover size and less aberration due to ions emitted far from the optical axis. The result is that the image of the entrance slit is better focused at the exit slit plane, and thus the entrance slit can be opened wider while still maintaining the same mass resolving power. This is an important advancement for any isotopic measurement that requires intermediate to high mass resolution, for example, Ti or Ca isotopes in meteoritic inclusions where M/ΔM = 12,000 is needed to adequately separate the isobars ^{48}Ti and ^{48}Ca [3,16]. It is worth noting that had these measurements been performed on the ims1290 with a duoplasmatron beam, one would expect results comparable to those obtained on the ims1270.
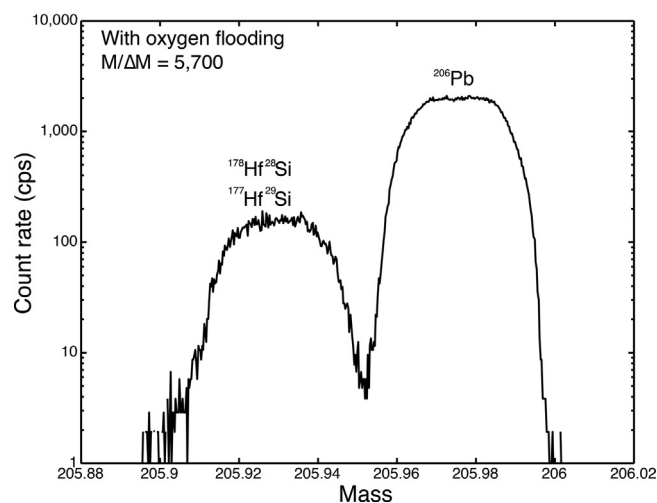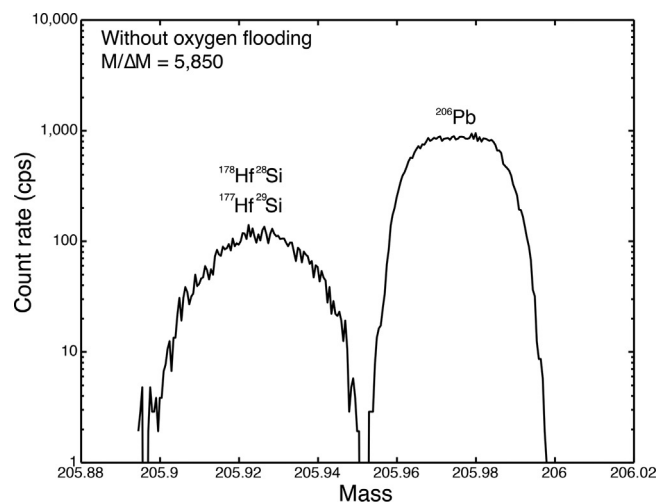
Fig. 6. Pb sensitivity characterized under the condition where U-Pb or Pb–Pb dating would be performed.

3.3. Lead sensitivity

The results of Pb sensitivity tests are shown in Fig. 6. A 10 nA primary beam bombarding a 91500 zircon standard and a secondary ion tuning condition corresponding to mass resolution (M/ΔM) of ~5800 result in a ^{206}Pb$^+$ count rate of 860 s^{-1} and 2030 s^{-1}, respectively, for analysis without and with oxygen flooding. This translates to 6.3 cps/ppm/nA and 14.7 cps/ppm/nA respectively. Although these values are comparable to those acquired by using a duoplasmatron on other ims1200 series ion microprobes [9,14], the fact that one could achieve higher sensitivity per unit area (e.g., 1.17 cps/ppm/nA/μm^2 and 0.03 cps/ppm/nA/μm^2 for Hyperion and duoplasmatron, respectively) in Pb isotopes with the Hyperion source makes possible significantly higher lateral resolution (at a few μm level), high precision zircon geochronology.

3.4. Mg isotopes: high precision, high reproducibility and high accuracy

Results of Mg isotopic analyses on a suite of standards measured at different spot sizes with the Hyperion source are shown in Fig. 7 and Table 2. Over the course of this analysis session, the external reproducibility of δ^{25}Mg and δ^{25}Mg is ~0.1–0.2‰ and ~0.3‰ (2σ), respectively, on all the standards, regardless of the primary beam intensities. The instrumental-fractionation-corrected Δ^{26}Mg* values for all isotopically normal standards average −0.03‰, 0.02‰

Table 2
Mg isotope data of standards measured with different beam intensities (5 nA, 10 nA and 15 nA).

	Ip	^{24}Mg (cps)	δ^{25}Mg	±2σ	δ^{26}Mg	±2σ	Δ^{26}Mg*	±2σ
Bsp_5nA@1	5.25	1.21E+08	−1.43	0.11	−2.61	0.13	0.07	0.24
Bsp_5nA@2.	5.25	1.21E+08	−1.53	0.08	−2.83	0.18	0.07	0.23
Bsp_5nA@3	5.26	1.22E+08	−1.57	0.10	−2.89	0.11	0.07	0.23
Bsp_5nA@4	5.24	1.21E+08	−1.57	0.12	−3.02	0.09	−0.05	0.24
Bsp_5nA@5	5.24	1.20E+08	−1.44	0.16	−2.85	0.18	−0.14	0.35
Bsp_5nA@6	5.25	1.20E+08	−1.28	0.08	−2.62	0.16	−0.23	0.22
Bsp_5nA@7	5.24	1.21E+08	−1.42	0.12	−2.71	0.17	−0.05	0.29
Bsp_5nA@8	5.25	1.21E+08	−1.40	0.14	−2.52	0.19	0.11	0.33
Bsp_5nA@9	5.26	1.20E+08	−1.38	0.11	−2.57	0.16	0.02	0.26
Bsp_5nA@10	5.26	1.20E+08	−1.56	0.13	−2.77	0.17	0.18	0.31
Scoliv_5nA@1	5.26	2.70E+08	−0.11	0.10	−0.16	0.15	−0.06	0.24
Scoliv_5nA@2	5.24	2.71E+08	−0.22	0.11	−0.31	0.19	0.00	0.28
Scoliv_5nA@3	5.26	2.70E+08	−0.21	0.10	−0.31	0.17	−0.02	0.26
Scoliv_5nA@4	5.25	2.70E+08	−0.23	0.13	−0.32	0.20	0.00	0.31
Scoliv_5nA@5	5.26	2.70E+08	−0.21	0.12	−0.28	0.19	0.02	0.30
Scoliv_5nA@6	5.25	2.67E+08	−0.04	0.10	0.04	0.21	0.00	0.28
Scoliv_5nA@7	5.25	2.69E+08	−0.23	0.14	−0.31	0.19	0.03	0.33
Scoliv_5nA@8	5.25	2.68E+08	−0.10	0.11	0.03	0.19	0.10	0.29
Scoliv_5nA@9	5.25	2.70E+08	−0.12	0.10	−0.25	0.16	−0.13	0.26
Scoliv_5nA@10	5.25	2.70E+08	−0.27	0.10	−0.42	0.17	0.00	0.25
SCpx_5nA@1	5.25	2.12E+08	3.78	0.11	7.52	0.17	−0.02	0.27
SCpx_5nA@2	5.25	2.14E+08	3.76	0.09	7.42	0.18	−0.06	0.26
SCpx_5nA@3	5.26	2.12E+08	3.78	0.08	7.63	0.18	0.09	0.24
SCpx_5nA@4	5.26	2.13E+08	3.65	0.12	7.33	0.15	0.05	0.28
SCpx_5nA@5	5.25	2.13E+08	3.78	0.11	7.51	0.14	−0.03	0.26
SCpx_5nA@6	5.26	2.12E+08	3.81	0.09	7.73	0.22	0.13	0.28
SCpx_5nA@7	5.25	2.11E+08	3.81	0.09	7.60	0.18	0.01	0.24
SCpx_5nA@8	5.25	2.11E+08	3.77	0.07	7.51	0.18	−0.01	0.22
SCpx_5nA@9	5.26	2.11E+08	3.87	0.11	7.56	0.13	−0.14	0.25
SCpx_5nA@10	5.27	2.10E+08	3.90	0.09	7.78	0.18	0.01	0.24
P10_5nA@1	5.26	4.91E+07	1.70	0.24	13.98	0.27	10.53	0.53
P10_5nA@2	5.26	4.93E+07	1.60	0.20	13.78	0.21	10.53	0.44
P10_5nA@3	5.26	4.92E+07	1.65	0.13	13.92	0.26	10.57	0.36
P10_5nA@4	5.27	4.97E+07	1.73	0.22	13.79	0.30	10.28	0.52
P10_5nA@5	5.27	4.84E+07	1.70	0.19	13.89	0.27	10.44	0.45
P10_5nA@6	5.27	4.88E+07	1.74	0.19	13.57	0.27	10.03	0.45
P10_5nA@7	5.26	4.95E+07	1.68	0.25	14.11	0.24	10.69	0.53
P10_5nA@8	5.26	4.94E+07	1.61	0.19	13.52	0.22	10.25	0.42
P10_5nA@9	5.26	4.95E+07	1.67	0.16	13.95	0.28	10.56	0.42
P10_5nA@10	5.27	4.97E+07	1.61	0.20	13.67	0.18	10.41	0.43
P0_5nA@1	5.27	4.60E+07	1.98	0.17	3.66	0.30	−0.35	0.44
P0_5nA@2	5.27	4.63E+07	1.82	0.22	3.52	0.36	−0.16	0.56
P0_5nA@3	5.27	4.63E+07	1.85	0.24	3.41	0.32	−0.33	0.56
P0_5nA@4	5.25	4.63E+07	1.55	0.19	3.30	0.27	0.14	0.46
P0_5nA@5	5.26	4.68E+07	1.83	0.20	2.99	0.34	−0.72	0.51
P0_5nA@6	5.26	4.60E+07	1.68	0.28	3.69	0.17	0.28	0.57
P0_5nA@7	5.27	4.59E+07	1.75	0.17	3.75	0.30	0.20	0.44
P0_5nA@8	5.25	4.59E+07	1.87	0.17	3.62	0.24	−0.17	0.41
P0_5nA@9	5.26	4.59E+07	1.83	0.18	3.42	0.32	−0.28	0.47
P0_5nA@10	5.25	4.53E+07	1.92	0.16	3.95	0.35	0.06	0.46
Bsp_10nA@1	10.29	242777700	−1.86	0.07	−3.54	0.10	−0.04	0.16
Bsp_10nA@2	10.35	2.47E+08	−1.97	0.11	−3.74	0.09	−0.02	0.24
Bsp_10nA@3	10.35	2.46E+08	−1.97	0.05	−3.65	0.09	0.07	0.14
Bsp_10nA@4	10.33	2.42E+08	−1.72	0.09	−3.37	0.12	−0.14	0.21
Bsp_10nA@5	10.34	2.42E+08	−1.68	0.09	−3.09	0.13	0.06	0.22
Bsp_10nA@6	10.35	2.41E+08	−1.77	0.05	−3.29	0.12	0.03	0.16
Bsp_10nA@7	10.37	2.44E+08	−1.75	0.09	−3.26	0.11	0.03	0.21
Bsp_10nA@8	10.39	2.42E+08	−1.87	0.10	−3.59	0.09	−0.07	0.21
Bsp_10nA@9	10.39	2.41E+08	−1.68	0.06	−3.07	0.08	0.08	0.14
Bsp_10nA@10	10.38	2.40E+08	−1.70	0.07	−3.08	0.12	0.12	0.19
SColiv_10nA@1	10.39	5.55E+08	−0.59	0.07	−1.03	0.14	−0.02	0.20
SColiv_10nA@2	10.41	5.55E+08	−0.44	0.10	−0.79	0.14	−0.06	0.24
SColiv_10nA@3	10.39	5.53E+08	−0.38	0.09	−0.65	0.10	−0.04	0.19
SColiv_10nA@4	10.38	5.48E+08	−0.47	0.09	−0.87	0.11	−0.08	0.21
SColiv_10nA@5	10.33	5.48E+08	−0.41	0.09	−0.68	0.14	−0.01	0.21
SColiv_10nA@6	10.32	5.49E+08	−0.54	0.08	−0.83	0.15	0.08	0.22
SColiv_10nA@7	10.34	5.56E+08	−0.73	0.07	−1.29	0.11	−0.01	0.17
SColiv_10nA@8	10.35	5.49E+08	−0.50	0.04	−0.81	0.11	0.03	0.14
SColiv_10nA@9	10.38	5.52E+08	−0.54	0.08	−0.96	0.15	−0.04	0.21
SColiv_10nA@10	10.40	5.52E+08	−0.54	0.07	−0.94	0.14	−0.01	0.20
SCpx_10nA@1	10.39	4.34E+08	3.40	0.09	6.84	0.14	0.05	0.22
SCpx_10nA@2	10.38	4.32E+08	3.50	0.07	7.03	0.15	0.04	0.20
SCpx_10nA@3	10.40	4.33E+08	3.50	0.07	7.02	0.14	0.03	0.20
SCpx_10nA@4	10.39	4.35E+08	3.41	0.06	6.83	0.14	0.01	0.19
SCpx_10nA@5	10.39	4.35E+08	3.49	0.07	6.87	0.11	−0.09	0.17

Table 2 (*Continued*)

	Ip	^{24}Mg (cps)	δ^{25}Mg	$\pm 2\sigma$	δ^{26}Mg	$\pm 2\sigma$	Δ^{26}Mg*	$\pm 2\sigma$
SCpx_10nA@6	10.40	4.34E+08	3.37	0.07	6.77	0.14	0.05	0.19
SCpx_10nA@7	10.39	4.36E+08	3.40	0.06	6.82	0.13	0.02	0.17
SCpx_10nA@8	10.38	4.33E+08	3.50	0.07	7.03	0.11	0.04	0.18
SCpx_10nA@9	10.39	4.36E+08	3.41	0.10	6.67	0.11	−0.14	0.22
SCpx_10nA@10	10.40	4.38E+08	3.25	0.08	6.53	0.13	0.02	0.21
P10_10nA@1	10.38	1.01E+08	1.43	0.12	13.11	0.17	10.17	0.29
P10_10nA@2	10.41	9.96E+07	1.46	0.16	13.21	0.22	10.23	0.38
P10_10nA@3	10.41	9.96E+07	1.44	0.08	13.31	0.21	10.35	0.26
P10_10nA@4	10.41	1.00E+08	1.37	0.13	13.07	0.18	10.26	0.30
P10_10nA@5	10.38	1.00E+08	1.34	0.14	13.23	0.14	10.46	0.29
P10_10nA@6	10.40	9.98E+07	1.55	0.15	13.20	0.15	10.03	0.33
P10_10nA@7	10.40	9.97E+07	1.44	0.08	13.33	0.17	10.37	0.23
P10_10nA@8	10.41	1.00E+08	1.40	0.12	13.06	0.08	10.17	0.25
P10_10nA@9	10.39	1.00E+08	1.41	0.14	13.24	0.11	10.34	0.29
P10_10nA@10	10.39	1.01E+08	1.53	0.08	13.07	0.10	9.94	0.19
P0_10nA@1	10.41	9.31E+07	1.54	0.09	3.31	0.12	0.16	0.21
P0_10nA@2	10.40	9.38E+07	1.53	0.12	3.20	0.14	0.07	0.27
P0_10nA@3	10.38	9.32E+07	1.56	0.15	3.01	0.21	−0.19	0.36
P0_10nA@4	10.41	9.38E+07	1.38	0.09	2.85	0.16	0.00	0.23
P0_10nA@5	10.39	9.43E+07	1.39	0.16	2.98	0.14	0.13	0.34
P0_10nA@6	10.37	9.45E+07	1.42	0.13	2.84	0.19	−0.08	0.31
P0_10nA@7	10.39	9.64E+07	1.16	0.10	2.63	0.17	0.23	0.25
P0_10nA@8	10.40	9.50E+07	1.39	0.09	3.10	0.15	0.24	0.23
P0_10nA@9	10.40	9.58E+07	1.40	0.11	2.74	0.17	−0.14	0.28
P0_10nA@10	10.42	9.62E+07	1.22	0.09	2.75	0.16	0.22	0.23
Bsp_15nA@1	14.97	3.45E+08	−2.14	0.05	−3.90	0.08	0.11	0.13
Bsp_15nA@2	14.96	3.47E+08	−2.01	0.05	−3.69	0.14	0.08	0.17
Bsp_15nA@3	14.98	3.46E+08	−2.07	0.08	−3.94	0.15	−0.07	0.21
Bsp_15nA@4	14.99	3.47E+08	−1.99	0.12	−3.80	0.09	−0.07	0.24
Bsp_15nA@5	14.99	3.48E+08	−1.93	0.08	−3.62	0.10	−0.01	0.19
Bsp_15nA@6	14.98	3.50E+08	−1.84	0.07	−3.36	0.09	0.06	0.16
Bsp_15nA@7	14.97	3.51E+08	−2.06	0.06	−3.81	0.10	0.06	0.15
Bsp_15nA@8	15.00	3.49E+08	−1.92	0.06	−3.55	0.10	0.03	0.16
Bsp_15nA@9	14.98	3.50E+08	−1.78	0.05	−3.35	0.13	−0.04	0.16
Bsp_15nA@10	14.97	3.35E+08	−1.65	0.07	−3.06	0.13	0.00	0.19
Scoliv_15nA@1	14.97	7.90E+08	−0.34	0.10	−0.54	0.17	−0.03	0.27
Scoliv_15nA@2	15.01	7.79E+08	−0.30	0.09	−0.47	0.14	−0.05	0.23
Scoliv_15nA@3	14.98	7.64E+08	−0.20	0.07	−0.21	0.15	0.02	0.21
Scoliv_15nA@4	14.94	7.89E+08	−0.38	0.08	−0.58	0.13	0.00	0.20
Scoliv_15nA@5	14.94	7.82E+08	−0.40	0.11	−0.67	0.17	−0.05	0.28
Scoliv_15nA@6	14.96	7.86E+08	−0.46	0.09	−0.74	0.13	−0.01	0.22
Scoliv_15nA@7	14.93	7.74E+08	−0.28	0.07	−0.41	0.17	−0.02	0.22
Scoliv_15nA@8	14.97	7.86E+08	−0.40	0.09	−0.71	0.16	−0.07	0.24
Scoliv_15nA@9	14.99	7.92E+08	−0.46	0.08	−0.78	0.15	−0.03	0.22
Scoliv_15nA@10	14.89	7.80E+08	−0.47	0.10	−0.78	0.15	−0.01	0.24
SCpx_15nA@1	14.84	6.17E+08	3.42	0.08	6.82	0.14	−0.01	0.21
SCpx_15nA@2	14.87	6.19E+08	3.41	0.09	6.81	0.16	0.00	0.23
SCpx_15nA@3	14.88	6.21E+08	3.44	0.07	6.83	0.17	−0.03	0.22
SCpx_15nA@4	14.85	6.22E+08	3.43	0.10	6.94	0.17	0.10	0.26
SCpx_15nA@5	14.87	6.32E+08	3.38	0.09	6.65	0.13	−0.09	0.22
SCpx_15nA@6	14.85	6.25E+08	3.35	0.08	6.73	0.13	0.04	0.20
SCpx_15nA@7	14.87	6.21E+08	3.46	0.07	6.93	0.13	0.03	0.19
SCpx_15nA@8	14.88	6.15E+08	3.61	0.09	7.17	0.14	−0.02	0.23
SCpx_15nA@9	14.87	6.20E+08	3.47	0.09	6.87	0.17	−0.06	0.25
SCpx_15nA@10	14.86	5.88E+08	3.46	0.07	6.93	0.17	0.04	0.22
P10_15nA@1	14.87	1.39E+08	1.59	0.10	13.71	0.15	10.46	0.24
P10_15nA@2	14.84	1.39E+08	1.52	0.11	13.44	0.08	10.33	0.23
P10_15nA@3	14.81	1.40E+08	1.40	0.11	13.47	0.19	10.60	0.29
P10_15nA@4	14.82	1.41E+08	1.32	0.08	13.24	0.19	10.50	0.25
P10_15nA@5	14.81	1.39E+08	1.39	0.08	13.30	0.12	10.44	0.19
P10_15nA@6	14.84	1.40E+08	1.40	0.08	13.24	0.18	10.35	0.24
P0_15nA@1	15.13	1.33E+08	1.37	0.13	2.96	0.16	0.13	0.30
P0_15nA@2	15.12	1.33E+08	1.60	0.08	3.26	0.11	−0.02	0.19
P0_15nA@3	15.11	1.34E+08	1.40	0.11	2.97	0.15	0.08	0.25
P0_15nA@4	15.11	1.35E+08	1.59	0.12	3.06	0.14	−0.19	0.28
P0_15nA@5	15.11	1.35E+08	1.48	0.15	2.95	0.13	−0.09	0.32
P0_15nA@6	15.11	1.36E+08	1.40	0.13	2.90	0.15	0.02	0.29
P0_15nA@7	15.12	1.35E+08	1.40	0.08	2.93	0.15	0.04	0.22
P0_15nA@8	15.12	1.35E+08	1.37	0.08	2.69	0.14	−0.13	0.21
P0_15nA@9	15.12	1.36E+08	1.34	0.14	2.91	0.10	0.15	0.29
P0_15nA@10	15.14	1.37E+08	1.35	0.12	2.80	0.17	0.01	0.30
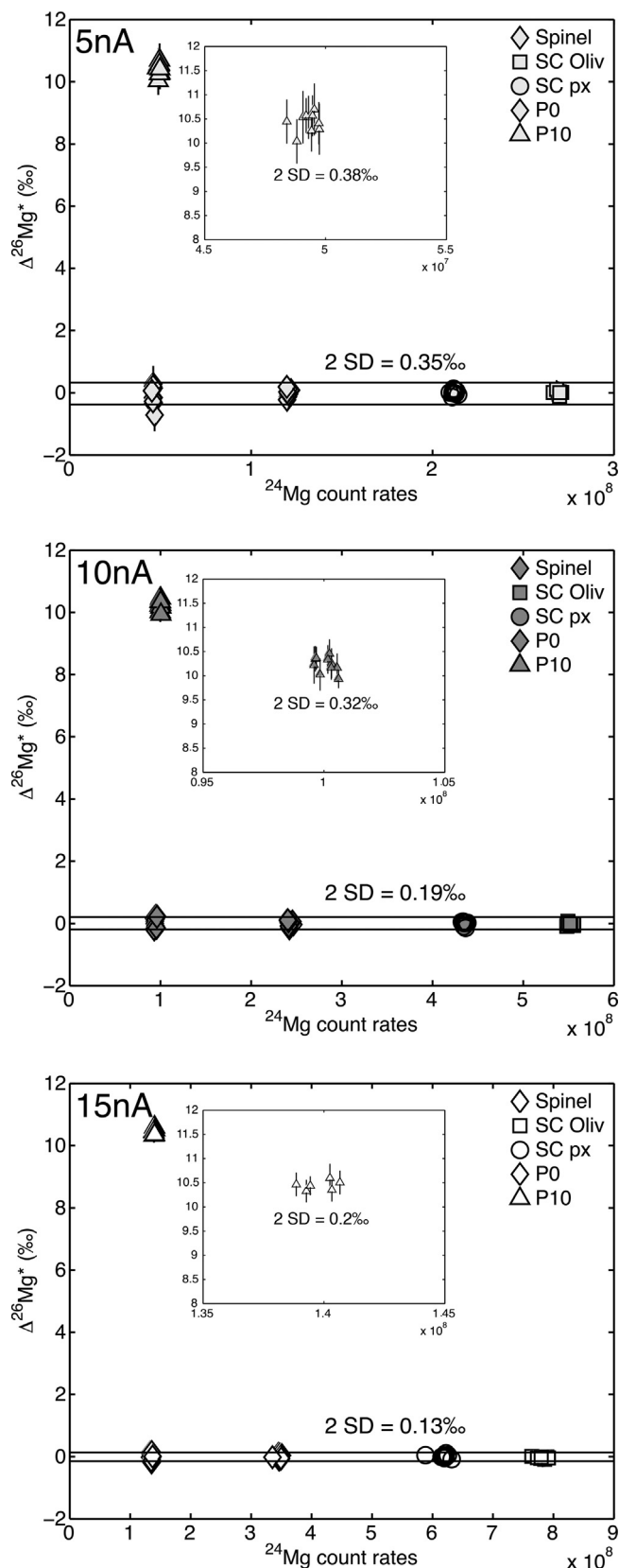
and 0‰, for 5, 10 and 15 nA, respectively, and the associated standard deviation (0.35‰, 0.19‰, and 0.13‰, all 2σ) reduces as the primary beam current increases. This level of reproducibility is comparable to those obtained on similar ion probes by using ~15–25 nA (φ ~ 20–25 μm) duoplasmatron beams [4,5,13]. Measurements of the P10 glass yield a ~10.23–10.43‰ excess in ^{26}Mg with external reproducibility ~0.2–0.3‰ (2σ), indicating excellent accuracy. The test demonstrates that the Hyperion source can deliver sufficient current into a small spot size for applications requiring both high precision, high accuracy isotopic measurements and high spatial resolution. Finally, an important observation in this exercise is that the primary beam intensity fluctuated by ~0.5% over 30 min, and by ~1% over the course of Mg isotopic analyses (~7 h); such stability is not generally observed with the duoplasmatron and would be highly desirable for long depth profile analyses where a constant erosion rate is useful.

4. Conclusion

The new RF plasma oxygen primary ion source provides a primary beam with current density ~10 times higher than the standard duoplasmatron does on a CAMECA *ims*1280HR ion microprobe. This improvement translates to higher spatial resolution at a given primary beam intensity, making it possible to perform isotopic analysis at smaller scale while maintaining analytical precision. Our evaluation of relative secondary ion transmission at different mass resolution settings shows a significant improvement over an instrument equipped with a duoplasmatron, demonstrating that the Hyperion-II source is also beneficial to measurements that require very high mass resolution. Finally, we show in this contribution that high precision, high accuracy Mg isotopic analysis can be realized with a spot size at least 2 times smaller than those used before.

Fig. 7. Magnesium isotopic measurements conducted by using a 5, 10, and 15 nA primary beam demonstrate high precision and high reproducibility. The spot size at each intensity can be seen in Fig. 2. See text for detailed explanation.

References

[1] A. Benninghoven, F. Rudenauer, H.W. Werner, Secondary Ion Mass Spectrometry: Basic Concepts, Instrumental Aspects, Applications and Trends, Wiley, New York, NY, 1987.
[2] J. Malherbe, F. Penen, M.-P. Isaure, et al., A new radio frequency plasma oxygen primary ion source on nano secondary ion mass spectrometry for improved lateral resolution and detection of electropositive elements at single cell level, Anal. Chem. 88 (2016) 7130–7136.
[3] M.-C. Liu, K.D. McKeegan, J.N. Goswami, et al., Isotopic records in CM hibonites: implications for timescales of mixing of isotope reservoirs in the solar nebula, Geochim. Cosmochim. Acta 73 (2009) 5051–5079.
[4] M.-C. Liu, M. Chaussidon, C. Göpel, T. Lee, A heterogeneous solar nebula as sampled by CM hibonite grains, Earth Planet. Sci. Lett. 327 (2012) 75–83.
[5] J. Villeneuve, M. Chaussidon, G. Libourel, Homogeneous distribution of ^{26}Al in the Solar System from the Mg isotopic composition of chondrules, Science 325 (2009) 985–988.
[6] T.M. Harrison, K.D. McKeegan, P. LeFort, Detection of inherited monazite in the Manaslu leucogranite by ^{208}Pb-^{232}Th ion microprobe dating: crystallization age and tectonic implications, Earth Planet. Sci. Lett. 133 (1995) 271–282.
[7] M.R. Reid, C.D. Coath, In situ U-Pb ages of zircons from the Bishop Tuff: no evidence for long crystal residence times, Geology 28 (2000) 443–446.

[8] W. Compston, I.S. Williams, C. Meyer, U-Pb geochronology of zircons form lunar Breccia 73217 using a sensitive high mass-resolution ion microprobe, Lunar and Planetary Science Conference Proceedings vol. 14 (1984) B525–B534.

[9] M. Schuhmacher, E. De Chambost, K.D. McKeegan, T.M. Harrison, H. Migeon, In situ dating of zircon with the CAMECA ims 1270, Secondary Ion Mass Spectrometry SIMS IX (1994) 919–922.

[10] M. Wiedenbeck, J.M. Hanchar, W.H. Peck, et al., Further characterization of the 91500 zircon crystal, Geostand. Geoanal. Res. 28 (2004) 9–39.

[11] E.J. Catanzaro, T.J. Murphy, E.L. Gardner, W.R. Shields, Absolute isotopic abundance ratios and atomic weights of magnesium, J. Res. Nat. Bur. Stand. 70a (1966) 453–458.

[12] A.M. Davis, F.M. Richter, R.A. Mendybaev, P.E. Janney, M. Wadhwa, K.D. McKeegan, Isotopic mass fractionation laws for magnesium and their effects on ^{26}Al-^{26}Mg systematics in solar system materials, Geochim. Cosmochim. Acta 158 (2015) 245–261.

[13] T.-H. Luu, M. Chaussidon, R.K. Mishra, et al., High precision Mg isotope measurements of meteoritic samples by secondary ion mass spectrometry, J. Anal. At. Spectrom. 28 (2013) 67–76.

[14] Y. Liu, X.-H. Li, Q.-L. Li, G.-Q. Tang, Q.-Z. Yin, Precise U-Pb zircon dating at a scale of <5 micron by the CAMECA 1280 SIMS using a Gaussian illumination probe, J. Anal. At. Spectrom. 26 (2011) 845–851.

[15] F.J. Stadermann, R.M. Walker, E. Zinner, Sub-micron isotopic measurements with the CAMECA NanoSIMS, Lunar and Planetary Science Conferences vol. 30 (1999) 1407 (abstract).

[16] A.J. Fahey, J.N. Goswami, K.D. McKeegan, E.K. Zinner, ^{26}Al, ^{244}Pu, ^{50}Ti, REE, and trace element abundances in hibonite grains from CM and CV meteorites, Geochim. Cosmochim. Acta 51 (1987) 329–350.